Measuring the thermal properties of anisotropic materials using beam-offset frequency domain thermoreflectance

Mizanur Rahman[1], Mohammadreza Shahzadeh[2], Philipp Braeuninger-Weimer[3], Stephan Hofmann[3], Olav Hellwig[4,5], Simone Pisana[1,2,*]

1. Department of Physics and Astronomy, York University, Toronto, Canada
2. Department of Electrical Engineering and Computer Science, York University, Toronto, Canada
3. Department of Engineering, University of Cambridge, Cambridge, United Kingdom
4. Institute of Physics, Chemnitz University of Technology, Chemnitz, Germany
5. Institute of Ion Beam Physics and Materials Research, Helmholtz-Zentrum Dresden-Rossendorf, Dresden, Germany

*. Corresponding author: simone.pisana@lassonde.yorku.ca

Thermoreflectance techniques have become popular to measure the thermal properties of thin films such as thermal conductivity and thermal boundary conductance (TBC). Varying the focused spot sizes of the beams increases the sensitivity to in-plane heat transport, enabling the characterization of thermally anisotropic materials. However, this requires realignment of the optics after each spot size adjustment. Offsetting the probe beam with respect to the pump beam and modulating over a wide range of frequencies (5 kHz to 50 MHz) yields better sensitivity to the thermophysical properties of anisotropic materials without varying the spot sizes. We demonstrate how beam-offset frequency domain thermoreflectance can be used to measure the in- and out-of-plane thermal conductivity as well as the TBC simultaneously from a single data set by working at reduced spot sizes. Lowering the laser spot size allows us to detect signals over a wide range of frequencies and use larger beam offsets, thanks to the increase in the thermoreflectance signal. We measure the anisotropic thermal properties of a range of materials, including single layer Graphene on SiO_2, which is of interest for novel electronic devices.

Introduction

Thermophysical properties of thin film materials are of great importance for thermal management in devices including transistors, lasers, sensors and plasmonic structures. Fundamentally, conductive heat transfer mechanisms at submicron length scales are still not completely understood, as they can involve non-equilibrium phenomena, multiple energy carriers, and are difficult to probe. In order to measure the thermal properties of thin films, optical pump probe methods including time-domain thermoreflectance (TDTR)[1,2] and frequency-domain thermoreflectance (FDTR)[3,4,5] are well recognized[6]. TDTR measures the temperature on the surface of a sample as function of the temporal delay between ultrafast pump and probe pulses, whereas FDTR measures the thermal lag on the surface of a sample with respect to the imposed heat flux from a modulated laser source. Both methods measure the surface reflectivity with a probe beam, which is related to the surface temperature through the principle of thermoreflectance. FDTR does not require the use of ultrafast lasers, electro-optic modulators and long optical delay stages, which makes it cost effective and simpler to implement. In both methods, the measured response is used to extract the thermal properties of the sample by fitting it to the solution of

the diffusive heat equation[1,2]. When the transport is non-diffusive, the model can either be interpreted to yield the effective property of interest, or be coupled to other models, such as the two-temperature model[7]. Typically thermoreflectance techniques are sensitive to out-of-plane thermal properties, but this is not a limitation when dealing with thermally isotropic materials.

2D layered materials are attractive candidates for device applications due to their unique combination of electrical, thermal and optical properties, and the great flexibility they provide in the creation of complex heterostructures[8-10]. Their intrinsic thermal properties are highly anisotropic and are still being investigated[11-13]. In spite of the high thermal conductivity commonly observed along the basal plane of 2D materials, out-of-plane thermal transport across a metallic contact or an insulating support is typically poor[14-18], leading to heat dissipation bottlenecks in electronic devices. Hence the investigation of heat transport in device-like structures is especially important.

The determination of the in-plane thermal conductivity of some anisotropic materials has been demonstrated using FDTR[14] and TDTR[19]. However, in order to increase the sensitivity to in-plane heat transport, the spot size of the beams needs to be varied[19], which requires the realignment of the optics. This can be a tedious task in systematic studies, and the accuracy obtained when performing a global fit to a spot size-dependent data set, which is necessary to obtain self-consistent results, is reduced by the overall experimental error. Alternatively, collecting data over a wide range of modulation frequencies also improves the sensitivities to in-plane transport, as this becomes important at relatively high frequencies (∼10 MHz). Beam-offset approaches, where the pump and probe beams are no longer coaxial, also increase the sensitivity to in-plane heat transport by directly sampling the surface temperature of the sample in the radial direction[2]. To obtain a more complete picture of the heat transport, the in-plane and out-of-plane thermal conductivities as well as the thermal boundary conductance (TBC) of these materials should be measured. Therefore, combining different approaches that increase the sensitivities to the various parameters of interest, as well as enriching the data sets by increasing the number of independent measurements, can provide a sufficiently complete data set to extract these unknowns simultaneously. Despite the importance of in-plane heat transport in 2D materials, there are only a few reports that demonstrate the determination of anisotropic thermal conductivity using FDTR[3,5,14,20]. These rely on either working with small spot sizes[3,5,14] or on beam offsetting[20]. However, if the experimental parameters are not associated with sufficiently high sensitivities, or the measurements do not span a sufficiently wide parametric range, the results can be plagued with relatively large error bars[20].

In this paper, we present a beam-offset FDTR (BO-FDTR) approach in which we combine the schemes outlined above in order to measure the thermal conductivity anisotropy and TBC from a single data set obtained at multiple beam offsets. We employ small spot sizes and modulate the pump beam over a wide range of frequencies up to 50 MHz. At high frequencies the signal to noise ratio is typically very low due to the thermal response of the sample (proportional to $f^{-1/2}$, where f is the modulation frequency), and the presence of coherent RF noise. The maximum reported modulation frequency in FDTR is 50 MHz for a coaxial geometry[14], though the use of heterodyne measurement techniques have extended detection frequencies to 200 MHz[3,21]. In BO-FDTR, the maximum reported modulation frequency is only 6 MHz because the signal strength further decays when the probe beam samples only

a portion of the thermal footprint given by the pump beam[20]. Here, we use spot sizes of about 1.4 µm, which yield high enough signals to allow measurements up to 50MHz at large beam offset values without the need of heterodyne measurement techniques. The coherent RF noise at high modulation frequencies can be reduced when necessary by taking reference noise measurements concurrently and subtracting the noise from the thermal signal, avoiding more complicated techniques such as heterodyning[4]. This approach allows us to reach large offsets above 1.4ω (where ω is the root-mean-square (RMS) beam radius at $1/e^2$).

Modeling and sensitivity analysis

The diffusive heat transport modeling framework used to determine the thermophysical properties of layered materials from thermoreflectance measurements is well established[1,2,19]. Here we only briefly outline the salient points that are more specific to BO-FDTR. The temperature fluctuation detected by the probe beam is given by [1,2]

$$\Delta T(f) = \frac{2\pi}{A_s}\int_0^\infty G(f,k)P(k)S(k)kdk \quad (1)$$

where $P(k)$ and $S(k)$ are the Hankel transforms of the intensity profiles of the Gaussian pump and probe beams, A_s is the total intensity of the sensing beam, and $G(f,k)$ is the Hankel transform of the frequency domain solution of the heat equation in multilayered media, with k being the Hankel transform variable. $G(f,k)$ is obtained iteratively using the thermophysical properties of all the layers comprising the sample, namely the thickness t, volumetric heat capacity C, and cross-plane and in-plane thermal conductivities $K_\perp$ and $K_\parallel$[19]. Thermal boundaries are modeled as layers having $t = 1$ nm, negligible heat capacity and equivalent $K_e = ht$, where h is the boundary conductance[1]. The pump beam is expressed as[1]

$$P(k) = A_p \exp\left(\frac{-\pi^2k^2\omega_p^2}{2}\right) \quad (2)$$

where A_p and ω_p are the total intensity and spot size of the pump beam. In the case of coaxial pump and probe beams the expression for $S(k)$ is equivalent to $P(k)$. In the case of sensing with an offset probe beam, $S(k)$ is defined as[2]

$$S(k) = \frac{A_s}{\pi}\exp\left\{-\left[\left(\frac{\sqrt{2}x_0}{\omega_s}\right)^2 + \left(\frac{\pi\omega_s k}{\sqrt{2}}\right)^2\right]\right\}\sum_{n=0}^{\infty}\frac{1}{(n!)^2}\left(\frac{\sqrt{2}x_0}{\omega_s}\right)^{2n} l_n\left(\frac{\omega_s k}{\sqrt{2}}\right) \quad (3)$$

where, x_0 is the offset between pump and probe beams, ω_s is the probe spot size and $l_n(x)$ is defined recursively as

$$l_{n+1}(x) = -\frac{1}{x}\left[(\pi^2x^3 - x)l_n(x) + \left(\frac{1}{4\pi^2} - x^2\right)l_n'(x) + \frac{x}{4\pi^2}l_n''(x)\right] \quad (4)$$

where $l_n'(x)$ and $l_n''(x)$ are the first and second derivative, respectively of $l_n(x)$, and $l_0 = \pi$.

We note that this model considers only diffusive heat transport. Small spot sizes and high modulation frequencies can lead to non-diffusive (quasi-ballistic) heat transport. Non-diffusive heat transport can take place when the heat carrier's mean free path becomes comparable with, or exceeds, the pump

spot size or the diffusive heat penetration depth $\ell = \sqrt{K/\pi C f}$[22,23]. Predicting when a departure from diffusive transport occurs can be complicated, as non-diffusive transport may take place anisotropically[22], according to heater geometry[23], or depend on the nature of the interface between two materials[24]. Analysis of experimental data in which non-diffusive transport takes place using a model that only considers diffusive heat transport often leads to obtaining thermal conductivities that fall below that of bulk values or frequency-dependent thermal properties. Therefore, care must be taken in interpreting the results of experiments when non-diffusive transport may take place.

The sensitivity to measurements to the parameters of interest, such as $K_\perp$, $K_\parallel$ and TBC depends in a complex way on the thermophysical properties of the layers comprising the sample, and insight on which property can be determined through measurement can be obtained by analysis of the measurement sensitivity as described below. For the case of a high thermal diffusivity thin film on a thermally isotropic bulk medium, sensitivity to measuring $K_\perp$ is enhanced at low modulation frequencies and large spot sizes, given the 1D out-of-plane isotherms obtained in this regime[25,26]. On the other hand, at high frequencies and small spot sizes, the isotherms are more spherical and the heat transport is more 3D, allowing for the determination of $K_\parallel$. The sensitivity to in-plane transport will be further enhanced when the thermal diffusivity of the substrate is much smaller than that of the thin film, leading to 2D in-plane transport. In most cases, sampling the in-plane transport will be enhanced when the pump and probe beams are offset.

The sensitivity of the measured phase signal θ (the phase of the complex temperature in eq. 1) due to a change in parameter x is defined as

$$S = \frac{d\,\theta}{d\ln x} \tag{5}$$

We considered at first a simple Al/Graphite system for sensitivity analysis as shown in figure 1 using the input values from table I. The sensitivity of the measured thermal phase signal due to various thermal parameters of a nominal Al/Graphite sample is shown in figures 1(a) and 1(b), for the concentric and 2 μm beam-offset cases, respectively, using an RMS spot size of 1.4 μm. By comparing the sensitivities at different offset values, we can determine that there is a high sensitivity to the anisotropic thermal conductivity of Graphite over a wide range of frequencies, as well as the TBC of Al/Graphite. These three parameters are distinguishable due to their dissimilar spectral sensitivity as the beam offset is varied. The sensitivity to $K_\parallel$ is enhanced at lower frequencies with respect to $K_\perp$ when the beams are offset, since the heat will diffuse with a longer thermal penetration depth in the radial direction where the probe beam can detect it. This is a common feature of BO-FDTR sensitivity curves. Without beam-offsetting, lateral heat spreading would only be sampled by the periphery of the probe beam, where the light intensity is low and the detected thermal phase changes by a small amount. Figures 1(c) and 1(d) show the sensitivities of the thermal phase signal to the in-plane thermal conductivity and out-of-plane thermal conductivity of Graphite, respectively, as the beam offset is varied from 0 to 2 μm. As shown, larger beam offsets comparable to the spot size are desirable to significantly increase the sensitivities to the in-plane transport.

Sample preparation

Graphene was synthesized by chemical vapor deposition (CVD) using Cu as catalyst and the subsequent transfer to SiO_2/Si substrates was performed using PMMA (poly(methyl methacrylate)) as a support and $FeCl_3$ chemical etching to remove the Cu[27]. Sapphire crystals (Crystech) were annealed in an oxidizing atmosphere before transducer deposition. A clean surface of highly-ordered pyrolytic Graphite crystals (SPI Supplies) was obtained by exfoliating the top layers with adhesive tape before transducer deposition. Al transducers were deposited by thermal evaporation or sputter deposition. White light interferometry or X-ray reflectivity was used to determine layer thickness, and 4-point probe electrical measurements for thermal conductivity via the Wiedemann-Franz law, respectively. The Al transducers for the Graphene and Graphite samples were 52 and 59 nm thick, respectively, and had thermal conductivities of 35.5 W/mK and 33 W/mK, respectively. These values may have been affected by small grain sizes and the presence of residual oxygen in the deposition chamber. We compared the results presented below with another Graphite sample having an Al transducer deposited elsewhere with thermal conductivity of 80 W/mK and obtained identical results within the experimental error. The Al transducers for the Sapphire samples were 55 nm thick and had a thermal conductivity of 170 W/mK.

Experimental setup

The experimental setup of BO-FDTR is shown in figure 2; it is based on two CW lasers operating at 515 nm (pump) and 785 nm (probe). Al transducers are used due to the high coefficient of thermoreflectance at the probe wavelength. The pump laser is directly modulated through its analog input and focused onto the surface of the sample using a 40X objective, whereas the probe beam remains unmodulated. Both beams pass through optical isolators to prevent back reflections into the lasers. A polarizing beam splitter (PBS), in conjunction with a quarter wave plate (QWP) maximizes the amount of light reaching the detector. To offset the probe beam, we use an actuator to steer a mirror. Care must be taken to ensure that the reflected probe beam is not cropped by optical elements in the sample-to-detector trajectory, and that it remains centered on the photodetector. Proper optical alignment and a focusing lens before the detector mitigate these issues. Alternatively, the pump beam can be steered with respect to the static probe's position.

After the absorption of the modulated pump beam, the periodic heat flux causes the surface temperature to change periodically at that frequency, but with an additional thermal phase $\theta_{thermal}$. Similar to other FDTR measurements we compare two measurements to extract the desired thermal phase from additional instrumental contributions that make up the measured phase. We refer to the first measurement as the thermal measurement (θ_1), performed by detecting the probe beam, and the second as the reference measurement (θ_2), performed by detecting the pump. Two optical band pass filters are used to separate the pump and probe beams before the photodetector. The contributions to the two FDTR measurements are: $\theta_1 = \theta_{thermal} + \theta_{optical} + \theta_{electrical} + \theta_{refernce}$ and $\theta_2 = \theta_{optical} + \theta_{electrical} + \theta_{reference}$. Therefore, $\theta_{thermal} = \theta_1 - \theta_2$, since both signals travel through the same optical and electrical paths.

Given that we work with small spot sizes, the accurate determination of spot sizes and beam offsets is critical to reduce sources of experimental error. Beam offsets and spot sizes are first characterized by

razor profiling using a piezoelectric stage. Pump and probe spot sizes are comparable, with $\omega \cong 1.4$ μm. However, since the focal position may vary slightly every time a sample is repositioned, we find that sufficient accuracy is obtained only when the spot sizes are determined at the focal position where a measurement is to be made. This is achieved by offsetting the probe beam with respect to the pump at high modulation frequencies to measure the combined response to the thermoreflectance signal, and finally fitting the obtained profile to a Gaussian curve to extract RMS spot sizes.

Results

We have measured the thermal properties of several anisotropic samples by modulating over a wide frequency range from 5 KHz to 50 MHz, and fit $K_{\perp}$, $K_{\parallel}$ and TBC concurrently at 2 μm beam offset. All of the fitted results in this work are summarized in table II. The experimental data for Al/Graphite with fitted analytical solution is shown in figure 3(a). The figure also shows the result of the model in the absence of the thermal boundary at the Al/Graphite interface, which shows a deviation from the data mirroring the shape of the sensitivity curve for TBC in fig 1(b). The fit yielded $K_{\perp}$=8±2 W/mK, $K_{\parallel}$=1,337±176 W/mK and the TBC of Al/Graphite of 41±5 MW/m^{2}K. These values agree well with literature data[2,19,28]. We check that there are no dependencies among the fit parameters by operating on the Variance-Covariance matrix. Note that all error bars indicated in this work are the standard errors obtained from the goodness of fit, and do not incorporate the propagation of uncertainties in the parameters that were held constant during the fit. To improve the standard error of the fit while maintaining self-consistent results, we concurrently fit measurements obtained at multiple offsets as shown in figure 3(b), yielding $K_{\perp}$=6.5±1 W/mK, $K_{\parallel}$=1,455±148 W/mK and TBC=47±1 MW/m^{2}K. As can be seen in figure 3(b), the thermal phase lag increases with increasing beam offset value, as indicated in the sensitivity curves of figure 1, in which all sensitivities are positive and increase with beam offset, i.e. given a set of thermal parameters, increasing the offset increases the change in thermal phase.

Similar measurements were performed on c-plane, a-plane and r-plane Sapphire to extract the anisotropic thermal conductivity and TBC. Sapphire is anisotropic with a larger thermal conductivity along the c-axis, the value depending on the level of impurities in the crystal. The sensitivity curves in figure 4(a) show frequency dependencies for the thermal parameters of interest to be quite distinct from each other and increasing with beam offset, indicating that each parameter can be individually determined. The data of figure 4(b) shows the development of a saddle point before 10 MHz for larger beam offsets, mimicking the increase in sensitivities of opposite sign for K and the TBC. There is a slight feature in our data at 5 MHz which coincides with the onset of coherent RF noise correction (which is performed for this sample at frequencies higher than 5 MHz). Our results for c-plane Sapphire, figure 4, show a larger $K_{\perp}$=50±1.2 W/mK as expected, the value being comparable to that obtained for high-quality crystals[29,30]. On the other hand, the values obtained for the a-plane and r-plane on two other crystals (Table II) do not show an appreciable anisotropy, as expected, since the in-plane and out-of-plane conductivities for these crystal planes are not aligned along the c-axis. The values of TBC of Al/Sapphire are in line with earlier reports[5], and indicate a lower conductance across the Al/r-plane interface, which is consistent with lower sound speeds recorded for this crystal face[31]. Lower sound

speeds indicate a flatter acoustic phonon dispersion relation, which dominates the contribution to the TBC.

Finally, we present the in-plane thermal conductivity measurements of single layer CVD Graphene (figure 5). The sample structure is Al/Graphene/SiO_2(296nm)/Si. The possibility of measuring the presence of monolayer Graphene between Al and the SiO_2/Si support is demonstrated in figure 5(a) where data in a region of the sample without Graphene is compared with a region with Graphene, yielding an appreciable difference as high as $\sim 5°$, well above the noise of the measurement. Figure 5(b) shows the sensitivity to measuring the $K_{\parallel}$ of Graphene and the TBC of the combined Al/Graphene/SiO_2 interface. Given the large anisotropy in Graphene favoring in-plane transport, the presence of the underlying thick, low-conductivity SiO_2 layer beneath it enhances the ability to assess $K_{\parallel}$. From the region where no Graphene was present we determine the TBC at the Al/SiO_2 interface (92 MW/m^2K) and at the SiO_2/Si interface (28 MW/m^2K), then we fix the TBC at the SiO_2/Si interface and all other parameters to fit $K_{\parallel}$ of Graphene and the combined TBC across the Al/Graphene/SiO_2 interfaces by performing beam-offset measurements at different locations of the sample (figures 5(c) and 5(d)). The TBC values at the Al/SiO2 and SiO_2/Si interfaces are consistent with those of other reports[15,25,32,33]. We model the Graphene layer as having a thickness of 0.35 nm and negligible out-of-plane thermal resistance, and treat this together with the TBC of Al/Graphene and the TBC of Graphene/SiO_2. The TBC across Al/Graphene/SiO_2 fit from the data at 9 different locations is 28±0.5 MW/m^2K, in line with other measurements[14,34]. This can be decomposed into a contribution of 47 MW/m^2K for the Al/Graphene interface (approximated from the TBC of Al/Graphite measured here), and 69 MW/m^2K for the Graphene/SiO_2 interface, in accordance with literature values[14,35]. The average value for $K_{\parallel}$ of Graphene obtained over 9 locations across the sample is 707±39 W/mK, which is very similar to the values reported in the literature for supported Graphene[14,36,37]. In all cases referenced, the single layer Graphene was supported on SiO_2, whereas in the work by Yang the Graphene was also covered by Al or Ti[14]. It's interesting to note that our reported value for $K_{\parallel}$ is in line with the literature in spite of the fact that the Graphene in this work was obtained by CVD growth, rather than mechanical exfoliation from Graphite. The similar values among these studies suggest that $K_{\parallel}$ in supported Graphene is predominantly limited by phonon scattering induced by the SiO_2 substrate, rather than grain boundary scattering within the Graphene layer or the presence of a metallic top layer. This is supported by Yang's observation that $K_{\parallel}$ was independent of Al or Ti contact metal[14], and their estimate that for $K_{\parallel} \sim 700$ W/mK the phonon mean free path in Graphene is $\sim$55 nm. This is substantially lower than the crystal domain size of 10-25 μm for the CVD Graphene sample used here or the flake sizes in the references cited, supporting the argument that the phonon mean free path is dominated by scattering induced by the SiO_2 substrate.

The results obtained here for Graphene demonstrate how BO-FDTR can be effective in determining $K_{\parallel}$ in substrate-supported 2D materials, which is typically challenging. We note that by beam-offsetting and high-frequency measurements we markedly reduced the uncertainties of the derived values. Yang's FDTR approach did not use beam-offsetting, and given the lower sensitivity in the coaxial geometry, it relies on a large number of measurements to reduce the statistical uncertainty of the derived values. Other techniques that have been used to determine the $K_{\parallel}$ in supported Graphene include suspended

microbridge geometries that are not amenable to systematic studies[36], or Raman/IR thermometry that do not independently measure the TBC[16,38,39] which affects the value and uncertainty of $K_{\parallel}$.

Conclusions

We have measured the in-plane, out-of-plane thermal conductivity and TBC simultaneously over a large range of thermal conductivity values (~5 W/mK to ~1,500 W/mK) in anisotropic samples. High sensitivities are obtained by modulating at high frequencies even at large beam offsets. We note that modulation frequencies of 50 MHz while at an offset of 1.4 times the spot size are the largest reported for beam offset FDTR and facilitate measurement of in-plane transport. The proposed approach to assessing the thermal properties of anisotropic materials will be helpful for device applications that take advantage of the promising qualities of emerging 2D materials.

Acknowledgments

M.R., M.S. and S.P. wish to acknowledge the Natural Sciences and Engineering Research Council of Canada, and York University for financial support. P.B.W. acknowledges funding from EPSRC Cambridge NanoDTC (EP/G037221/1). S.H. acknowledges funding from EPSRC, UK (EP/K016636/1).

References

[1] D. G. Cahill, Review of Scientific Instruments **75**, 5119 (2004).
[2] J. P. Feser, D. G. Cahill, Review of Scientific Instruments **83**, 104901 (2012).
[3] J. Yang, C. Maragliano, A. J. Schmidt, Review of Scientific Instruments **84**, 104904 (2013).
[4] K. T. Regner, S. Majumdar, J. A. Malen, Review of Scientific Instruments **84**, 064901 (2013).
[5] A. J. Schmidt, R. Cheaito, M. Chiesa, Review of Scientific Instruments **80**, 094901 (2009).
[6] D. G. Cahill, P. V. Braun, G. Chen, D. R. Clarke, S. Fan, K. E. Goodson, P. Keblinski, W. P. King, G. D. Mahan, A. Majumdar, H. J. Maris, S. R. Phillpot, E. Pop, L. Shi., Applied Physics Reviews **1**, 011305 (2014).
[7] R. B. Wilson, J. P. Feser, G. T. Hohensee, D. G. Cahill, Physical Review B **88**, 144305 (2013).
[8] K. S. Novoselov, A. Mishchenko, A. Carvalho, A. H. Castro Neto, Science **353**, Issue 6298, 461 (2016).
[9] Z. Sun, A. Martinez, F. Wang, Nature Photonics **10**, 227 (2016).
[10] F. Withers, O. Del Pozo-Zamudio, A. Mishchenko, A. P. Rooney, A. Gholinia, K. Watanabe, T. Taniguchi, S. J. Haigh, A. K. Geim, A. I. Tartakovskii, K. S. Novoselov, Nature Materials **14**, 301 (2015).
[11] A. A. Balandin, Nature Materials **10**, 569 (2011).
[12] Z. Luo, J. Maassen, Y. Deng, Y. Du, R. P. Garrelts, M. S. Lundstrom, P. D. Ye, X. Xu, Nature Communications **6**, 8572 (2015).
[13] J. Liu, G.-M. Choi, D. G. Cahill, Journal of Applied Physics **116**, 233107 (2014).
[14] J. Yang, E. Ziade, C. Maragliano, R. Crowder, X. Wang, M. Stefancich, M. Chiesa, A. K. Swan, A. J. Schmidt, Journal of Applied Physics **116**, 023515 (2014).
[15] A. J. Schmidt, K. C. Collins, A. J. Minnich, G. Chen, Journal of Applied Physics **107**, 104907 (2010).
[16] M. Freitag, M. Steiner, Y. Martin, V. Perebeinos, Z. Chen, J. C. Tsang, Ph. Avouris, Nano Letters **9**, 1883 (2009).
[17] A. D. Liao, J. Z. Wu, X. Wang, K. Tahy, D. Jena, H. Dai, E. Pop, Physical Review Letters **106**, 256801 (2011).

[18] M.-H. Bae, Z.-Y. Ong, D. Estrada, E. Pop, Nano Letters **10**, 4787 (2010).
[19] A. J. Schmidt, X. Chen, G. Chen, Review of Scientific Instruments **79**, 114902 (2008).
[20] D. Rodin, S. K. Yee, Review of Scientific Instruments **88**, 014902 (2017).
[21] K. T. Regner, D. P. Sellan, Z. Su, C. H. Amon, A. J. McGaughey, J. A. Malen, Nature Communications **4**, 1640 (2013).
[22] R. B. Wilson, D. G. Cahill, Nature Communications **5**, 5075 (2014).
[23] C. Hua, A. J. Minnich, Physical Review B **97**, 014307 (2018).
[24] C. Hua, X. Chen, N. K. Ravichandran, A. J. Minnich, Physical Review B **95**, 205423 (2017).
[25] P. E. Hopkins, J. R. Serrano, L. M. Phinney, S. P. Kearny, T. W. Grasser, C. T. Harris, Journal of Heat Transfer **132**, 081302 (2010).
[26] L. Belliard, C. Frétigny, E. Charron, S. Vincent, B. Perrin, D. Fournier, Journal of Applied Physics **117**, 065306 (2015).
[27] P. Braeuninger-Weimer, B. Brennan, A. J. Pollard, S. Hofmann**,** Chemistry of Materials **28**, 8905 (2016).
[28] www.2spi.com/item/430hp-ab/hopg-momentive-performance.
[29] St.Burghartz, B.Schulz, Journal of Nuclear Materials **212–215 Part B**, 1065 (1994).
[30] E. R. Dobrovinskaya, L. A. Lytvynov, V. Pishchik, Sapphire: Material, Manufacturing, Applications (Springer).
[31] J. M. Winey, Y. M. Gupta, Journal of Applied Physics **90**, 3109 (2001).
[32] J. A. Malen, K. Baheti, T. Tong, Y. Zhao, J. A. Hudgings, A. Majumdar, Journal of Heat Transfer **113**, 081601 (2011).
[33] C. Zhang, W. Zhao, K. Bi, J. Ma, J. Wang, Z. Ni, Z. Ni, Y. Chen, Carbon **64**, 61 (2013).
[34] Y. K. Koh, M.-H. Bae, D. G. Cahill, E. Pop, Nano Letters **10**, 4363 (2010).
[35] K. F. Mak, C. H. Lui, T. F. Heinz, Applied Physics Letters **97**, 221904 (2010).
[36] J. H. Seol, I. Jo, A. L. Moore, L. Lindsay, Z. H. Aitken, M. T. Pettes, X. Li, Z. Ya, Science **328**, 213 (2010).
[37] M.-H. Bae, Z. Li, Z. Aksamija, P. N. Martin, F. Xiong, Z.-Y. Ong, I. Knezevic, E. Pop, Nature Communications **4**, 1734 (2013).
[38] W. Cai, A. L. Moore, Y. Zhu, X. Li, S. Chen, L. Shi, R. S. Ruoff, Nano Letters **10**, 1645 (2010).
[39] J.-U. Lee, D. Yoon, H. Kim, S. W. Lee, H. Cheong, Physical Review B **83**, 081419(R) (2011).
[40] E. H. Buyco, F. E. Davis, Journal of Chemical and Engineering Data **15**, 518 (1970).
[41] W. DeSorbo, W. W. Tyler, Journal of Chemical Physics **21**, 1660 (1953).
[42] J. Horbach, W. Kob, K. Binder, Journal of Physical Chemistry B **103**, 4104 (1999).
[43] V. M. Glazov, A. S. Pashinkin, High Temperature **39**, 413 (2001).
[44] D. A. Ditmars, S. Ishihara, S. S. Chang, G. Bernstein, Journal of Research of the National Bureau of Standards **87**, 159 (1982).
[45] D. G. Cahill, Review of Scientific Instruments **61**, 802 (1990).
[46] G. A. Slack, Journal of Applied Physics **35**, 3460 (1964).

Tables

Table I: Nominal values for fitting and sensitivity analysis. Thickness values are obtained by white light interferometry or X-Ray reflectivity. The K for Al is assumed isotropic and determined by four point probe. *: the value of K for Al for these samples may have been affected by small grain sizes and the presence of residual oxygen in the deposition chamber. Blank values indicate a property that was obtained from fits to the experimental data.

Property	Graphite Sample	Graphene Sample	Sapphire Samples
Thickness of Al (nm)	59	52	55
C_v of Al (MJ/m^3K)	2.42[40]	2.42[40]	2.42[40]
$K_\perp$ of Al (W/mK)	33*	35.5*	170
$K_\parallel$ of Al (W/mK)	33*	35.5*	170
C_v of Substrate (MJ/m^3K)	1.6[41]	SiO_2=1.59[42], Si=1.64[43]	3.03[44]
$K_\perp$ of Substrate (W/mK)	5.7[19]	SiO_2=1.32[45], Si=145[46]	-
$K_\parallel$ Substrate (W/mK)	1950[19]	SiO_2=1.32[45], Si=145[46]	-
TBC of Al/Substrate (MW/m^2K)	50[15]	-	-

Table II: Measured values for different anisotropic samples. *: the error bar here represents the confidence interval obtained from 9 measurements. †: the TBC in this case is that of the Al/Graphene/SiO_2 structure.

Sample	$K_\perp$(W/mK)	$K_\parallel$ (W/mK)	TBC with Al (MW/m^2K)
Graphite	6.5±1	1,455±148	47±1
c-plane Sapphire	50±1.2	35±0.6	134±3
a-plane Sapphire	39±2	37±1.1	167±11
r-plane Sapphire	41±2	37±1.2	118±4
Single layer Graphene		707±39*	28±0.5†

Figure Captions

Figure 1: (a) and (b) depict the sensitivity of the measured thermal phase to changes in various parameters at 0 µm and 2 µm beam offsets respectively, (c) and (d) show the sensitivities to in-plane and out-of-plane thermal conductivity of Graphite, respectively, for several values of beam offsets.

Figure 2: Schematic diagram of Beam-Offset FDTR.

Figure 3: (a) Experimental phase data (symbols) with fitted analytical solution (solid lines) of the Al/Graphite sample at 2 µm beam offset. For comparison, the dashed line is the model prediction for the same structure, but without the TBC present at the Al/Graphite interface. Panel (b) shows aggregate data and global fit using 3 beam offset values: 0 µm (black), 1.5 µm (red) and 2 µm (navy).

Figure 4: (a): Sensitivity to $K_{\perp}$, $K_{\parallel}$ of c-Sapphire and TBC across Al/c-Sapphire interfaces, for several values of beam offsets. (b) Experimental phase data (symbols) with fitted analytical solution (solid lines) for the Al/c-Sapphire sample. The beam offset values were 1 µm (black), 1.5 µm (red) and 2 µm (navy).

Figure 5: (a) Experimental phase data at 0 µm beam offset for the Al/Graphene/SiO_2/Si sample on an area containing Graphene (black symbols) compared with an area that does not contain Graphene (red symbols). (b): Sensitivity to $K_{\parallel}$ of Graphene and TBC across Al/Graphene/SiO_2 interfaces for the Al/Graphene/SiO_2/Si sample, for several values of beam offsets of 1 µm (black), 1.5 µm (red) and 2 µm (navy). (c): Experimental phase data (symbols) with fitted analytical solution (solid lines) for the Al/Graphene/SiO_2/Si sample. The beam-offset values were 0 µm (black), 1 µm (red) and 1.5 µm (navy). (d): $K_{\parallel}$ of single layer Graphene for the structure Al/Graphene/SiO_2/Si extracted from different locations in the sample.

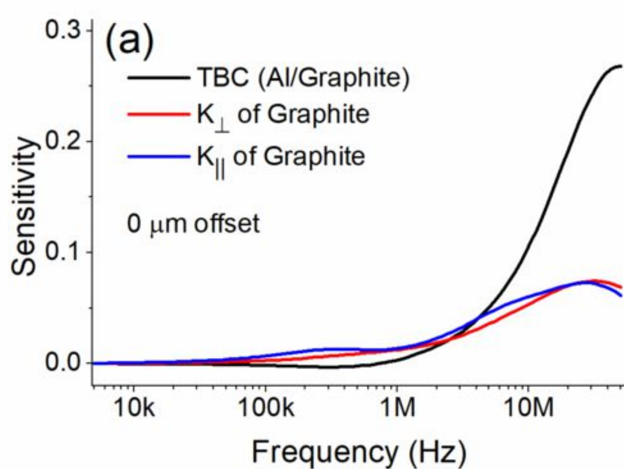
(a)
TBC (Al/Graphite)
$K_\perp$ of Graphite
$K_{||}$ of Graphite
0 μm offset
Sensitivity
Frequency (Hz)
0.3
0.2
0.1
0.0
10k
100k
1M
10M
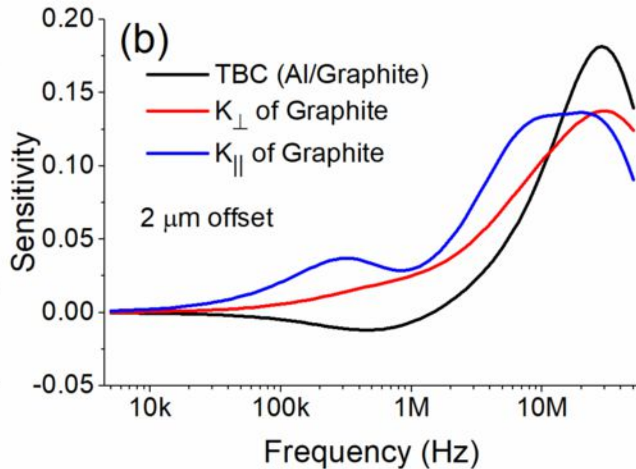
(b)
TBC (Al/Graphite)
$K_\perp$ of Graphite
$K_{||}$ of Graphite
2 μm offset
Sensitivity
Frequency (Hz)
0.20
0.15
0.10
0.05
0.00
-0.05
10k
100k
1M
10M
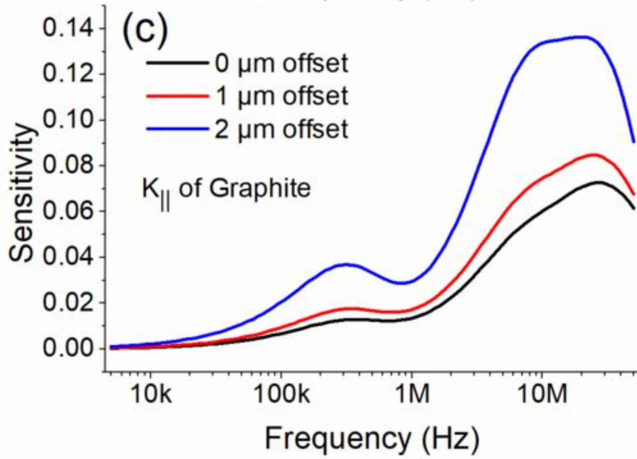
(c)
0 μm offset
1 μm offset
2 μm offset
$K_{||}$ of Graphite
Sensitivity
Frequency (Hz)
0.14
0.12
0.10
0.08
0.06
0.04
0.02
0.00
10k
100k
1M
10M
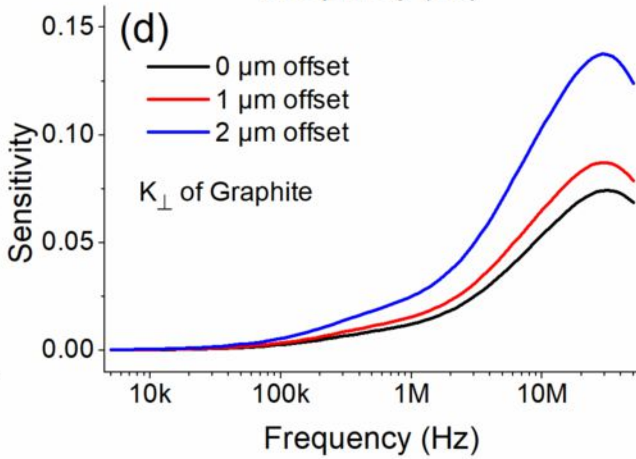
(d)
0 μm offset
1 μm offset
2 μm offset
$K_\perp$ of Graphite
Sensitivity
Frequency (Hz)
0.15
0.10
0.05
0.00
10k
100k
1M
10M

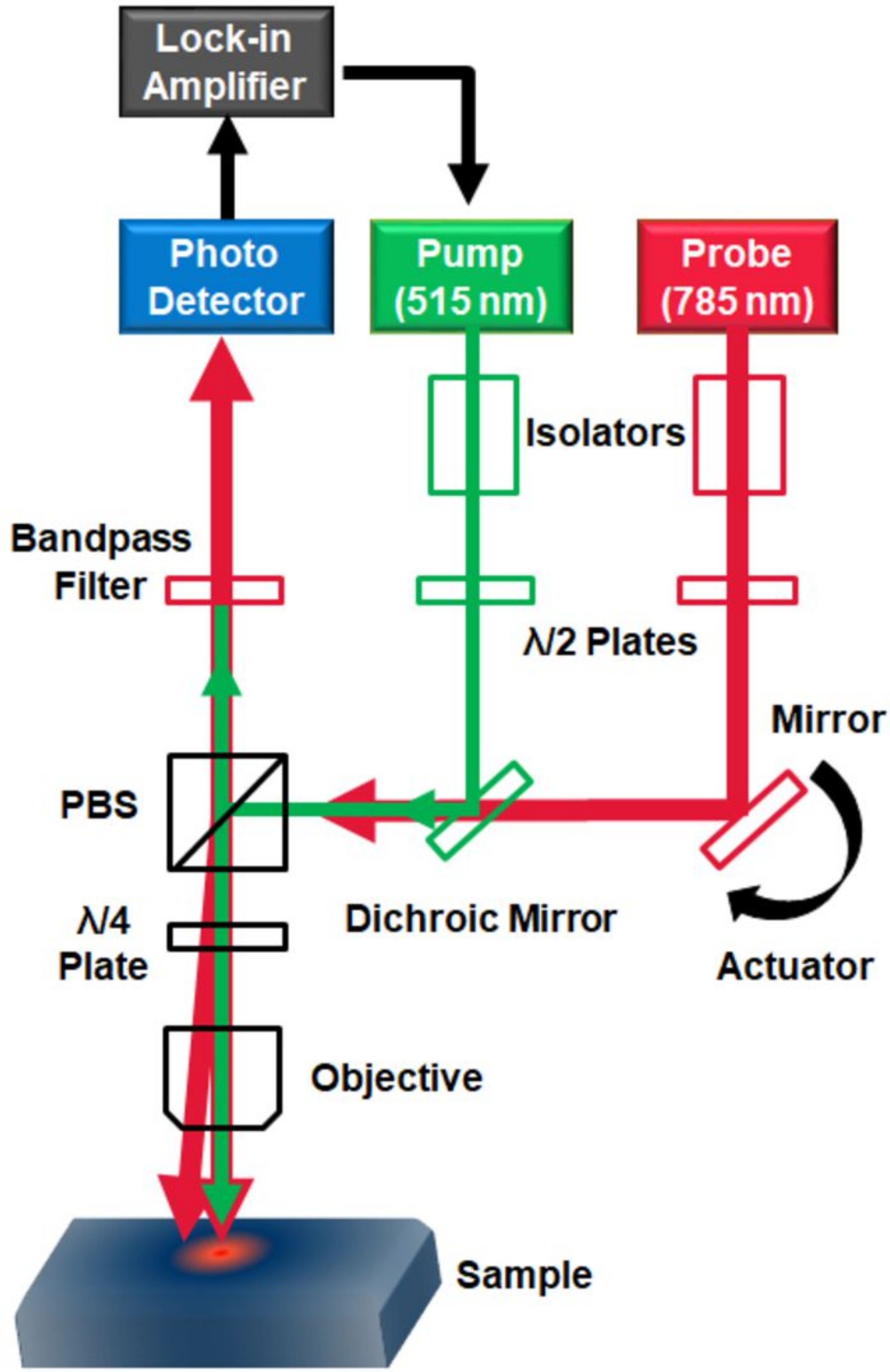
Lock-in
Amplifier
Photo
Detector
Pump
(515 nm)
Probe
(785 nm)
Isolators
Bandpass
Filter
λ/2 Plates
Mirror
PBS
Dichroic Mirror
λ/4
Plate
Actuator
Objective
Sample

(a)

Data
Fit
Without TBC

Phase (degree)

0
-10
-20
-30
-40
-50
-60
-70

100k
1M
10M

Frequency (Hz)

(b)

Data
Fit

Phase (degree)

0
-10
-20
-30
-40
-50
-60
-70

100k
1M
10M

Frequency (Hz)

(a)

Sensitivity

0.15
0.10
0.05
0.00
-0.05
-0.10
-0.15

10k
100k
1M
10M

Frequency (Hz)

TBC of Al/ c-Sapphire
$K_{\perp}$ of c-Sapphire
$K_{||}$ of c-Sapphire

(b)

Phase (degree)

0
-10
-20
-30
-40

10k
100k
1M
10M

Frequency (Hz)

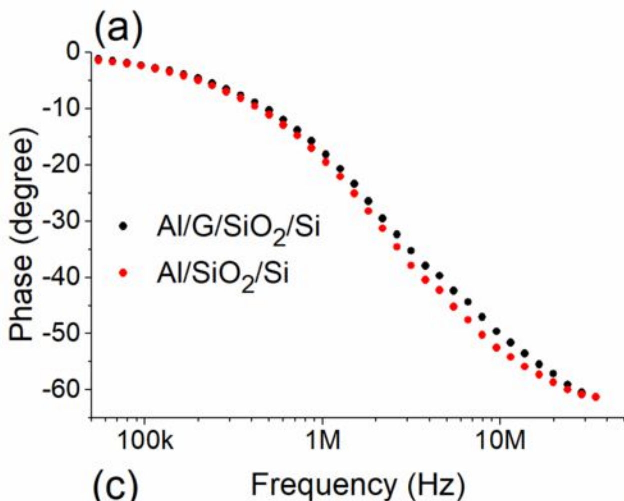
(a)
Phase (degree)
Frequency (Hz)
Al/G/SiO2/Si
Al/SiO2/Si
0
-10
-20
-30
-40
-50
-60
100k
1M
10M

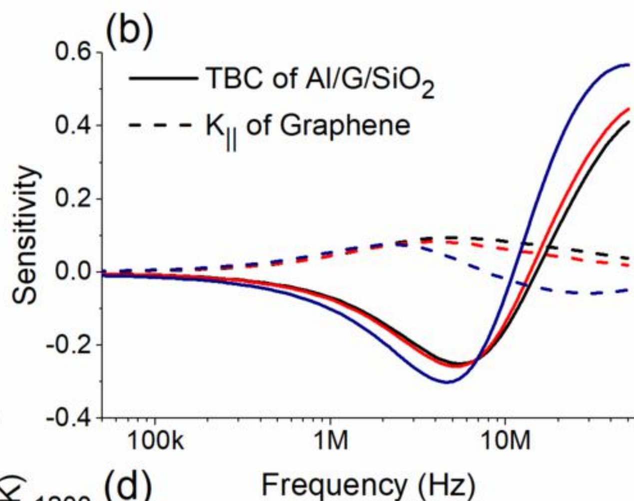
(b)
TBC of Al/G/SiO2
K|| of Graphene
Sensitivity
Frequency (Hz)
0.6
0.4
0.2
0.0
-0.2
-0.4
100k
1M
10M

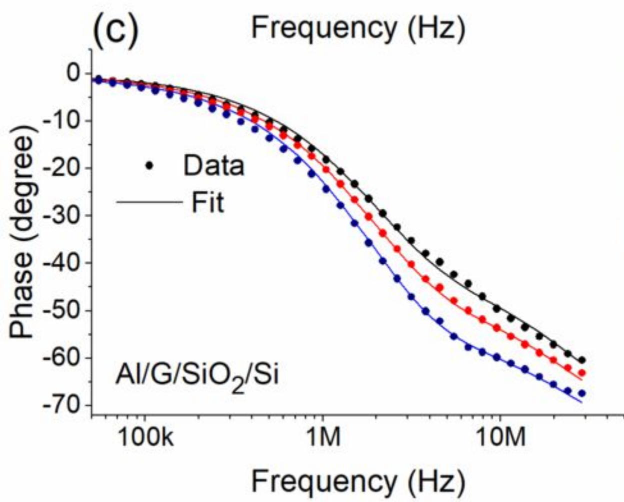
(c)
Data
Fit
Al/G/SiO2/Si
Phase (degree)
Frequency (Hz)
0
-10
-20
-30
-40
-50
-60
-70
100k
1M
10M

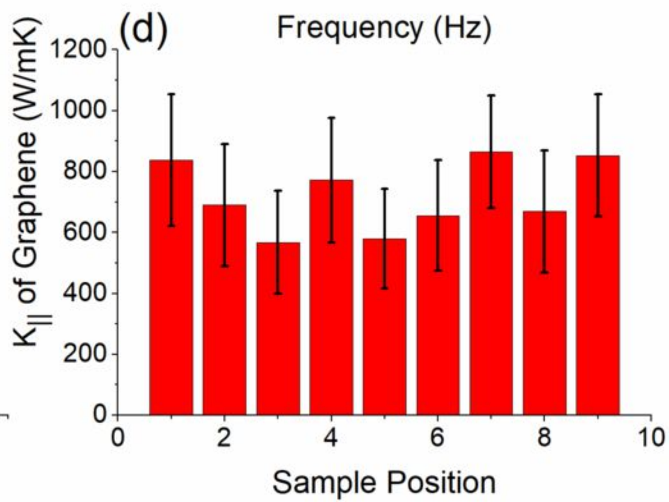
(d)
K|| of Graphene (W/mK)
Sample Position
1200
1000
800
600
400
200
0
0
2
4
6
8
10